Sadegh Pour-Ali, Alireza Kiani-Rashid, Abolfazl Babakhani
Materials and Metallurgical Engineering Department, Faculty of Engineering, Ferdowsi University of Mashhad, Mashhad, Iran

# Improved corrosion inhibition of 3-amino-1,2,4-triazole on mild steel electrode in HCl solution using surface nanocrystallization



A nanocrystalline surface layer with average grain size of 77 nm was produced on mild steel through a wire brushing process. Its corrosion behavior was studied in the absence and presence of 3-amino-1,2,4-triazole (3-AT) as corrosion inhibitor. Although the increase in the inhibitor concentration shows a positive effect on inhibition efficiency of micro- and nano-grained surfaces, this effect is more remarkable for the sample with a nanocrystalline surface layer. In addition, in the presence of the optimum concentration of 3-AT, temperature increment has a more negative effect on the sample with a microcrystalline surface layer. The results also revealed that due to enhanced adsorption of 3-AT inhibitor and formation of a protective layer with a high polarization resistance, the inhibition effect of 3-AT increased as the grain size decreased from microcrystalline to nanocrystalline.

**Keywords:** Mild steel; TEM; EIS; Corrosion inhibition; Surface nanocrystallization

## 1. Introduction

The role of surface structure is undeniable in the majority of engineering applications. Fatigue fracture, wear and corrosion are important examples of engineering failures which are very sensitive to the properties of the material's surface [1, 2]. There are different methods for improvement of surface performance, including electroplating [3], electroless plating [4], organic coatings [5], anodic oxidation [6], hot dipping [7], thermal spraying [8], diamond-like coatings (DLCs) [9], laser surface engineering [10] and surface nanocrystallization (SNC) [11, 12]. Among these methods, SNC has attracted considerable scientific attention in recent decades. The reason for that is that the ultrafine crystallite structure of a nanocrystalline layer, i.e. presence of a large fraction of atoms located in the interface regions, causes significant improvements in selected mechanical [13], physical and chemical properties compared to their coarse grained counterparts [14]. It is common to produce an ultrafine-grained surface through severe plastic deformation (SPD) processes. Shot peening [13], surface mechanical grinding treatment [15], friction sliding [16] and wire brushing [17] are among the most important SPD methods for SNC treatments. These methods are successful in forming ultrafine surface grains with mean grain sizes smaller than 1 μm in various kinds of metallic materials. Among the above SPD processes, wire brushing is relatively simple, flexible and applicable for different classes of materials. This technique is also capable of modifying the surface microstructure and removing mill scales which, in turn, helps more effective adsorption of corrosion inhibitors and improvement of coating adhesion [5, 18].

As has been widely reported, nanocrystallization of a coarse-grained polycrystalline material provides a new approach to the improvement of properties without changing its chemical composition. The small grain size and the high volume fraction of grain boundaries may result in corrosion behavior different from that of polycrystalline materials [19, 20]. Based on the report by Li et al. [21] on the SNC of low carbon steels, grain sizes smaller than 35 nm showed a strong effect on the electrochemical corrosion behavior so that the corrosion rate of the nanocrystallized low carbon steel increased with the decreasing of grain size. They claimed that this effect can be attributed to the increased number of active sites caused by SNC treatment. On the other hand, Luo and co-workers [22] investigated the corrosion rate of nanocrystalline copper in NaOH solution and reported that changes in grain size from polycrystalline to nanocrystalline, led to little effect on the overall corrosion resistance of copper samples. Balasubramaniam and Mishra [23] studied the electrochemical corrosion behavior of nanocrystalline nickel in 1 M $H_2SO_4$ solution. Their findings revealed that the zero current potential, passive current density and breakdown potential are generally increased with decrease in grain size. Hao et al. [24] also found that the corrosion resistance of AISI 316SS in sodium sulfate solutions greatly improved after SNC processing. According to the study of the effect of SNC treatment on the corrosion performance of 304SS by Wang et al. [25], the nanocrystalline surface caused by sandblasting and annealing treatment exhibited considerably higher resistance to corrosion compared to the annealed samples. Ralston and Birbilis [26] claimed that improved corrosion resistance from grain refinement is generally attributed to improvement in passive film stability, which can be the result of increased rates of diffusion in nano- or fine-grained structures. On the other hand, increased rates of corrosion as grain size decreases are attributed to passive film destabilization. Based on the findings reported by Oguzie et al. [19, 27, 28] and Umoren et al. [29, 30], both the corrosion and corrosion inhibition mechanisms are affected by the SNC process. In the absence of corrosion inhibitors, this process diminishes the

corrosion resistance of iron ingots by accelerating the kinetics of the anodic metal dissolution; however, nanocrystallization has a greater inhibiting effect and leads to more corrosion resistance upon introduction of corrosion inhibitors. As is clear from the mentioned studies, there is no general consensus in the literature about the effect of grain size on corrosion resistance. Nonetheless, all reports demonstrate that the higher grain boundary content in the nanocrystalline specimens increases the amount of the atoms that take part in the corrosion reactions which occur at the mild steel/electrolyte interface. In accordance with the altering in surface activity, it can be claimed that the SNC treatment may affect the extent of adsorption and surface coverage of corrosion inhibitors on the metal surface. Hence, the aim of the present work is to study the effect of SNC of mild steel on the inhibition efficiency of 3-amino-1,2,4-triazole (3-AT) as a corrosion inhibitor in HCl solution. For this purpose, wire brushing was used to achieve a surface layer with ultrafine grains. Transmission electron microscopy (TEM) and X-ray diffraction (XRD) were used to determine the surface grain size. Afterwards, the corrosion inhibition of different concentrations of 3-AT on mild steel coupons with coarse- and ultrafine-grained surfaces was evaluated by potentiodynamic polarization and electrochemical impedance spectroscopy (EIS) in 0.1 M HCl solution. It is also noticeable that there is no investigation on the effect of SNC of mild steel on inhibition efficiency of 3-AT in the literature.

Table 1. Chemical composition (wt.%) of mild steel coupon.

| C | Si | Mn | Cr | Mo | Ni | S | P | Fe |
|---|---|---|---|---|---|---|---|---|
| 0.19 | 0.11 | 0.41 | 0.30 | 0.14 | 0.24 | 0.01 | 0.02 | Bal. |

## 2. Experimental procedure

### 2.1. Materials

Mild steel plates for all experiments were purchased from Esfahan's Mobarakeh Steel Co., Iran. The chemical composition of the mild steel coupons is shown in Table 1. 3-AT with a purity of >95.0 wt.% was purchased from Sigma-Aldrich. The molecular structure of 3-AT is given in Fig. 1. The test electrolyte, 0.1 M HCl, was prepared from Merck reagent and deionized water.

### 2.2. Surface treatment

The annealed mild steel coupons with average grain size of 65 μm were mechanically ground down to 1 000 grit emery paper (Ref sample), then washed in deionized water and immediately dried with hot air. Afterward, the coupons were wire brushed at room temperature with a feeding speed of $5\ mm \cdot s^{-1}$, load of 50 N and brush rotational speed of 8 000 rpm (WB sample). This treatment is shown in Fig. 2.

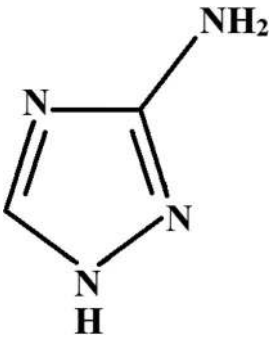


Fig. 1. Molecular structure of 3-AT.

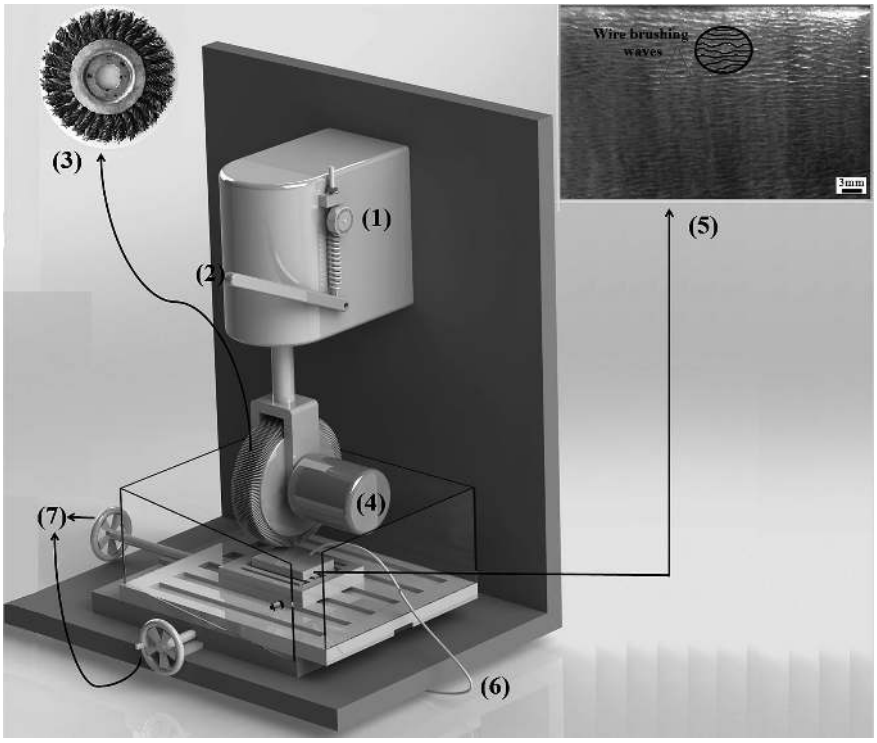


Fig. 2. Illustration of wire brushing process: (1) spring balance, (2) force application, (3) wheel brush, (4) electric motor, (5) wire brushed coupon, (6) coolant agent, and (7) transverse and longitudinal motions.

The diameters of wire and brush parts were 600 µm and 5.8 cm, respectively. In order to prevent the wrapping or crushing of wires during high speed wire brushing, a particular wheel brush design, shown in Fig. 2, was used. This brush was provided by Jahan Brush Co., Iran. In the wire brushing process, each coupon was processed for two passes, and the coupon was rotated by 180° before the second pass. This procedure was done to obtain a uniform deformation.

### 2.3. Surface analysis

Surface morphology of the treated coupon was characterized by means of transmission electron microscopy (TEM, Tecnai G2, Netherlands). The thickness of the deformation affected zone for the wire brushed sample was determined by microhardness measurement (Buehler hardness tester with 25 g load) and scanning electron microscopy analysis (SEM, S360, Oxford). X-ray diffraction (XRD) studies were carried out using a Philips X'Pert-Pro instrument operated with Co-$K_\alpha$ radiation ($\lambda = 0.1789$ nm) at a scan rate of 0.05° $s^{-1}$ in the range of 40 – 130° and 0.02° step size. Average grain size was estimated according to the Williamson–Hall equation [31 – 33]:

$$\beta_r \cos\theta = (k\lambda/D) + \mu \sin\theta \quad (1)$$

where, $D$ is the grain size, $k$ is the Scherer factor which is between 0.89 to 1.39 depending on the shape and size of the grain (it is usually considered 0.9), $\mu$ is representative of strain, $\lambda$ and $\theta$ are the wavelength of the irradiated X-ray and Bragg's angle, respectively. The $\beta_r$ in Eq. (1) is equal to $(\beta_0^2 - \beta_i^2)^{0.5}$, in which $\beta_0$ and $\beta_i$ are the widths of each wave in the half of maximum height in ultrafine grain and coarse grain samples, respectively. With plotting the variation of $\beta_r \cos\theta$ in terms of $\sin\theta$ and fitting the best regression, the average size of the ultrafine grains formed within the surface layer was calculated.

### 2.4. Corrosion evaluation

Electrochemical impedance spectroscopy (EIS) and potentiodynamic polarization are two classical electrochemical techniques which are used to determine the characteristics of corrosion inhibitors. An EG&G potentiostat (Model 273A) and a Solartron frequency response analyzer (Model SI 1255) were employed to run the corrosion tests in a conventional three electrode configuration. The working electrode, with 2.25 $cm^2$ exposed area, was made by cold mounting of a mild steel coupon with a self-cure epoxy resin. The working electrodes were mechanically ground with emery papers down to 1 200 grade, then washed with distilled water and finally dried with hot air flow. A saturated

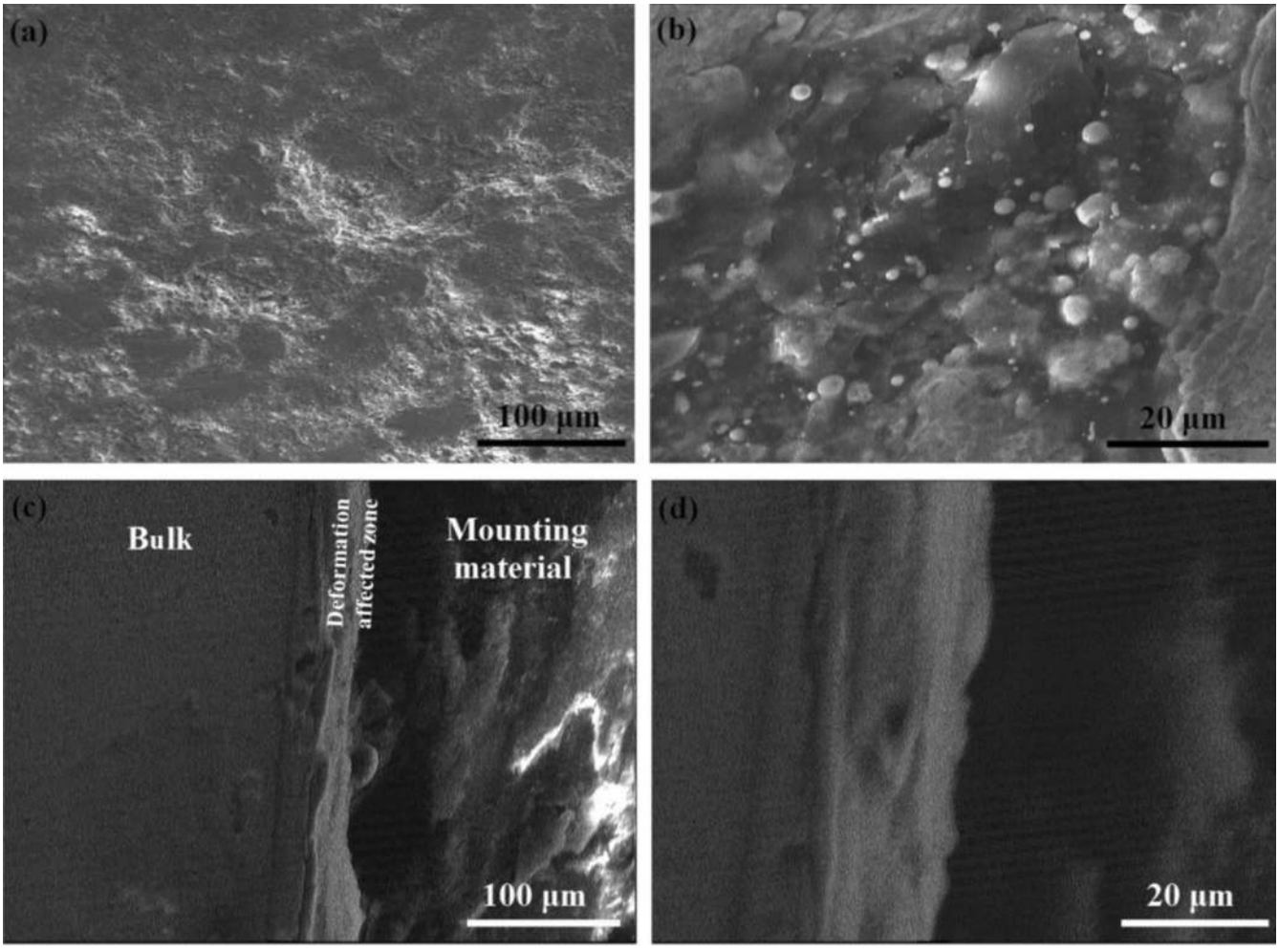


Fig. 3. SEM images of (a and b) the surface, and (c and d) the cross-section of a wire brushed coupon in different magnifications.

calomel electrode (SCE) and a platinum wire were also used as reference and auxiliary electrodes, respectively. Before each electrochemical measurement, the working electrode was immersed for 75 min in solution to obtain a steady state open circuit potential (OCP). Potentiodynamic polarizations were carried out at a sweep rate of 1 $mV \cdot s^{-1}$ in which the scanning range was almost –300 to +300 mV around the OCP. The impedance measurements were performed in the frequency range of 100 kHz to 10 mHz using an AC overpotential with amplitude of 10 mV around OCP. In the electrochemical tests, blank solution was 0.1 M HCl and four inhibitor concentrations of 25, 50, 100 and 200 $mg \cdot L^{-1}$ were also chosen.

## 3. Results and discussion

### 3.1. Morphology of wire brushed surface and hardness measurement

Figure 3 displays SEM images from the surface and cross-section of a WB coupon. Different areas of the surface of WB coupon have identical deformation-affected zone. As clearly seen in Fig. 2, the treated coupon shows a bright metallic luster. Wire brushing waves can be also observed on the surface of WB. High magnification microscopy with TEM reveals that the wire brushing produced an ultrafine-grained surface with a nearly uniform distribution (see Fig. 4). According to TEM analysis, the average grain size for WB is estimated to be 80 nm. This value is in agreement with the results obtained by Tao et al. [34] and Song et al. [17].

Figure 5 shows the XRD patterns of the surface of WB and annealed steel coupon as reference. The broadening of peaks in the wire brushed state can be an indication of grain refinement to an ultrafine size [35]. The result of the Williamson–Hall analysis of the treated sample, presented in Fig. 6, is reasonably in agreement with TEM observations. In this way, the average surface grain size of WB is calculated to be 74 nm. Thus, these results clearly verify the formation of ultrafine grains on the surface of the wire brushed mild steel coupon.

Figure 7 depicts the variation of microhardness from surface to the bulk material for Ref and WB coupons. The results indicate that near the surface of treated coupon, hardness is significantly increased. In the case of WB, the nanostructured surface layer leads to an increase in hardness up to 1.65 times comparing to its core or the coarse-grain sample (Ref). Because a sudden jump is observed in hardness, it can be claimed that the ultrafine surface grain layer is not thick (less than 50 μm) [36]. Based on scanning electron microscopy (Fig. 3) and hardness measurements, the mean thickness of this layer is about 20 μm.

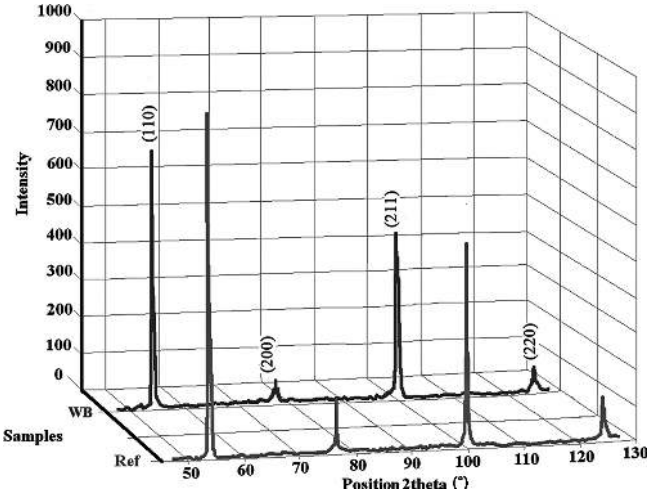


Fig. 5. XRD patterns of annealed and wire brushed mild steel coupons.

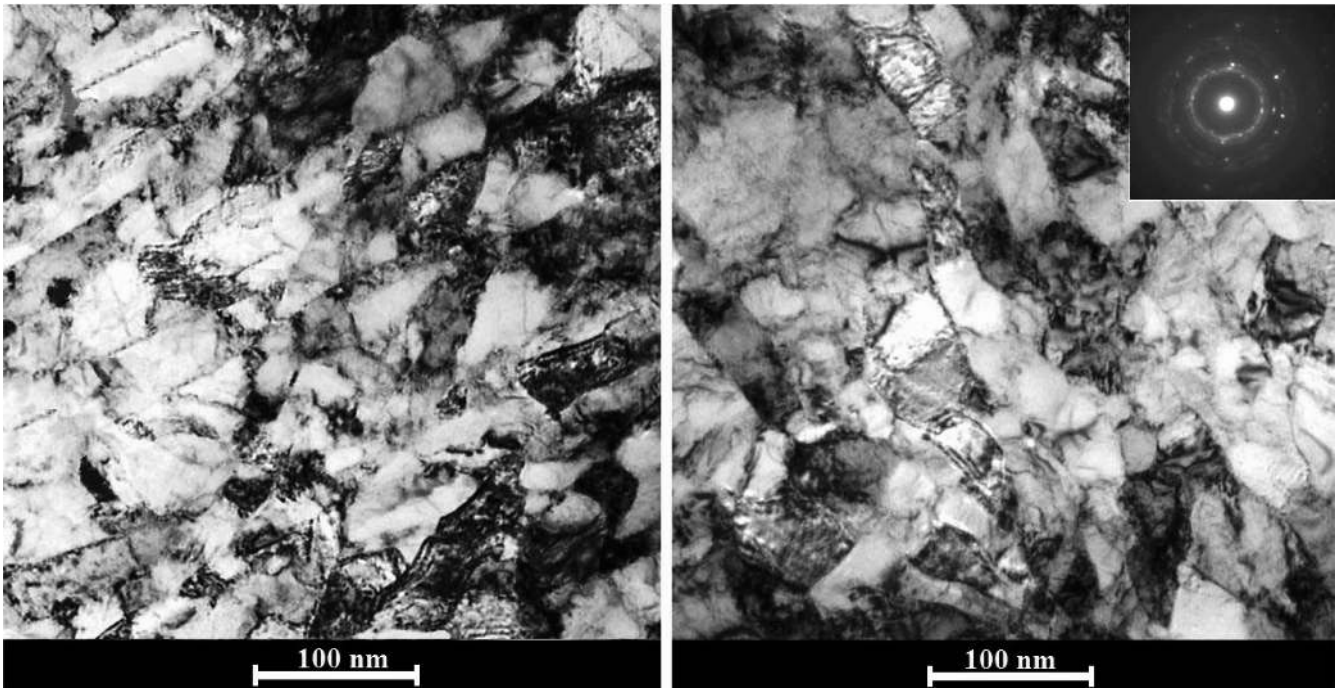


Fig. 4. TEM observations of nanocrystalline grains obtained from the surface layer of wire brushed coupon.

The values of $R_a$ (arithmetic mean deviation of the assessed roughness profile) and $R_t$ (total height of roughness profile) for all samples are presented in Table 2. As can be seen, through the wire brushing process, the $R_a$ value (which can be considered as the representative parameter of surface roughness) is increased from 0.24 μm (Ref) to 14.43 μm (WB).

### 3.2. Corrosion performance

#### 3.2.1. Effect of surface nanocrystallization and inhibitor concentration

Figure 8 shows potentiodynamic polarization plots for Ref and WB coupons in 0.1 M HCl at 26 °C with different concentrations of 3-AT. Electrochemical parameters derived from these plots including corrosion potential ($E_{corr}$), corrosion current density ($i_{corr}$) and cathodic ($\beta_c$) and anodic Tafel slopes ($\beta_a$), which were measured using Tafel extrapolation of the anodic and cathodic lines, are listed in Table 3. Values of surface coverage ($\theta$) and inhibition efficiency ($\%\eta_i$) are calculated from the following electrochemical equations [37]:

$$\theta = \frac{i_{corr(blank)} - i_{corr(inh)}}{i_{corr(blank)}} \quad (2)$$

$$\%\eta_i = \theta \times 100 \quad (3)$$

Where $i_{corr(blank)}$ and $i_{corr(inh)}$ are corrosion current densities in the absence and presence of 3-AT. It should be noted that for analysis of polarization curves which do not show completely linear Tafel behavior (e. g. anodic or cathodic Tafel slopes of bulk solutions), a specific method was employed [38]. As can be assessed from Fig. 8 and Table 3, corrosion performance of Ref and WB samples is improved in the

Table 2. Surface roughness parameters of Ref and WB coupons.

| Sample | $R_a$ (μm) | $R_t$ (μm) |
|---|---|---|
| Ref | 0.24 | 1.15 |
| WB | 14.43 | 18.59 |

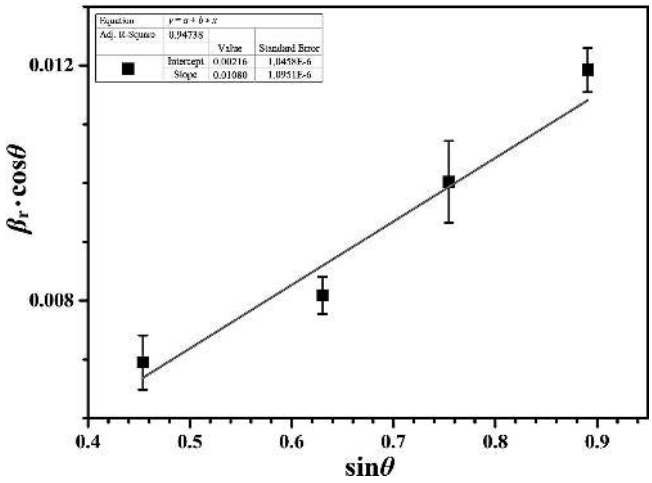


Fig. 6. Williamson–Hall analysis of wire brushed sample.

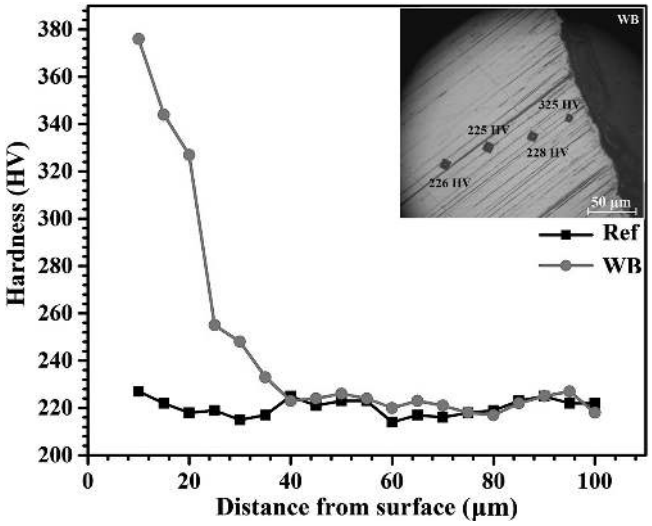


Fig. 7. Microhardness profiles for the annealed and wire brushed coupons from the surface towards the core.

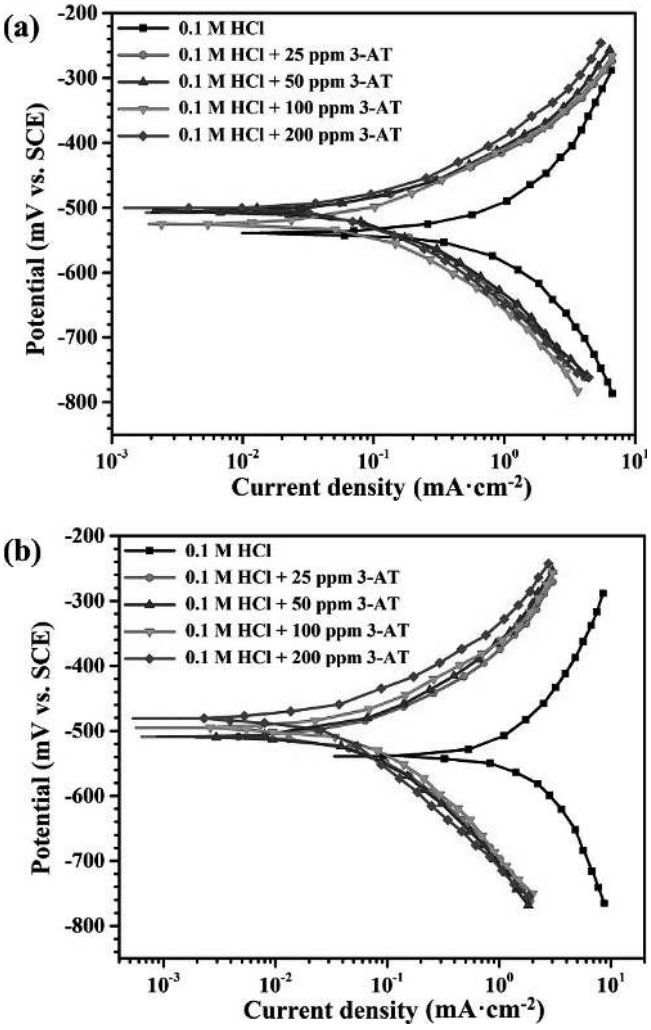


Fig. 8. Polarization curves for (a) Ref and (b) WB samples in 0.1 M HCl without and with various concentrations of 3-AT.

presence of 3-AT. Presence of this inhibitor leads to a significant decrease in the corrosion rate of both samples; however, it is more remarkable for the WB coupon so that this specimen with nanocrystalline surface layer obtains superior inhibition efficiencies i. e. more than 90 %. Assessment of Fig. 8 shows that both net anodic and net cathodic current densities decrease by increasing the inhibitor concentration. This fact means that this inhibitor can partially retard anodic (e. g. metal dissolution) and cathodic (e. g. hydrogen evolution) reactions. Adsorption of inhibitor molecules onto the metal surface and blocking the active sites is an accepted mechanism for such observations [39]. According to Table 3, the corrosion rate of mild steel coupon in 0.1 M HCl solution is remarkably increased after SNC process. This behavior is directly related to extraordinary increase in the grain boundaries as high energetic sites. Similar arguments have been reported in previous studies [21–23]. On the other hand, iron dissolution of WB is dramatically decreased with small addition of corrosion inhibitor so that presence of 25 ppm of 3-AT leads to ~90 % inhibition efficiency. Thus, it can be claimed that surface nanocrystallization which provide enhanced grain boundary density on the surface of mild steel coupon increases the 3-AT adsorption. Such phenomenon can be responsible for low corrosion rate of WB coupon in the presence of 3-AT. Though the Tafel slopes do not follow a definite trend, the variation of $\beta_c$ and $\beta_a$ with alteration of inhibitor concentration and surface microstructure reveals the effect of these variables on the kinetics of anodic and cathodic reactions.

Electrochemical impedance spectroscopy (EIS) is a powerful technique that has been used in understanding the mechanisms of corrosion, passivation and charge transfer phenomena of metals and alloys in aggressive environments [40]. In our study, EIS was employed in order to confirm the kinetics and electrochemical characteristics of iron dissolution for Ref and WB coupons in the absence and presence of 3-AT. Figure 9 represents the Nyquist and Bode plots of Ref and WB coupons in the test solutions at 26 °C. The Nyquist plots contain a semicircle at high frequencies which is directly related to the polarization resistance including charge transfer resistance, diffuse layer resistance, the accumulated species at the metal/solution interface and the resistance of inhibitor film at the steel surface. The Bode phase angle plots show only one time constant (single maximum in Fig. 9c and f) which correspond to one semicircle capacitive loop in the Nyquist plots. The semicircles in Nyquist plots are considered to be depressed type which usually result from surface roughness and degree of polycrystallinity [41]. Bigger semicircle diameter and/or higher impedance modulus mean higher polarization resistance which is obtained in the presence of higher concentrations of corrosion inhibitor. In the absence of 3-AT, the values for WB coupon are smaller than the Ref one, implying that polarization resistance is decreased by decreasing the grain size from micron to nanometer scale. These conditions are completely different in the presence of 3-AT so that higher semicircle diameters or higher polarization resistances for WB sample can be attributed to the uniform and/or dense inhibitor adsorption on the most active sites. Experimental EIS data were fitted to an electrical equivalent circuit illustrated in Fig. 9d. This circuit reveals electrolyte resistance, $R_s$, constant phase element of double layer, $CPE_{dl}$, and polarization resistance, $R_p$. Constant phase element (CPE) was used as the alternative to capacitor to study the metal/solution interface more accurate. The impedance function of the CPE is represented by the following expression.

$$Z_{CPE} = \frac{1}{P(i\omega)^n} \tag{4}$$

Where, $P$ is the magnitude of the CPE, $\omega$ the angular frequency, and $n$ as the deviation parameter. The behavior of the CPE can be explained on the basis of values of $n$. Generally, if the value of $n$ equals +1, 0 and –1, the CPE behaves as resistance, capacitance and inductance, respectively. Double layer capacitance ($C_{dl}$) was calculated using the following equation [42]:

$$C_{dl} = \frac{P\omega^{(n-1)}}{\sin(n(\pi/2))} \tag{5}$$

Inhibition efficiency values ($\%\eta_p$) were also calculated from the impedance data by comparing the polarization resistance of Ref and WB coupons with ($R_p$) and without ($R_p^\circ$) 3-AT using the following formula:

$$\%\eta_p = \frac{R_p - R_p^\circ}{R_p} \times 100 \tag{6}$$

Table 3. Electrochemical parameters obtained from the polarization curves of Ref and WB coupons in the test solutions.

| Specimen | Concentration (ppm) | $E_{corr}$ (mV vs. SCE) | $i_{corr}$ (mA · cm$^{-2}$) | Tafel slopes (mV · decade$^{-1}$) | | $\theta$ | $\%\eta_i$ |
|---|---|---|---|---|---|---|---|
| | | | | $\beta_a$ | $-\beta_c$ | | |
| Ref | Blank | –539 | 0.88 | 204 | 191 | – | – |
| | 25 | –509 | 0.13 | 101 | 133 | 0.85 | 85 |
| | 50 | –507 | 0.13 | 97 | 142 | 0.85 | 85 |
| | 100 | –528 | 0.12 | 93 | 139 | 0.86 | 86 |
| | 200 | –501 | 0.11 | 102 | 152 | 0.88 | 88 |
| WB | Blank | –542 | 1.26 | 178 | 151 | – | – |
| | 25 | –510 | 0.12 | 109 | 124 | 0.90 | 90 |
| | 50 | –510 | 0.12 | 103 | 119 | 0.90 | 90 |
| | 100 | –495 | 0.08 | 110 | 127 | 0.94 | 94 |
| | 200 | –482 | 0.05 | 101 | 134 | 0.96 | 96 |

The calculated values of $n$ with other impedance parameters such as $R_s$, $R_p$, $C_{dl}$, $\%\eta_p$ and $P$ are given in Table 4. Examination of these results clearly reveals that WB coupon shows two different behaviors in the presence and absence of 3-AT compared with Ref one. With comparing the results in the blank solution, it can be found that WB coupon shows lower $R_p$ and higher $C_{dl}$ values which is attributed to the higher fraction of surface active sites and higher relative permittivity, respectively. This finding is consistent with previous studies [43].

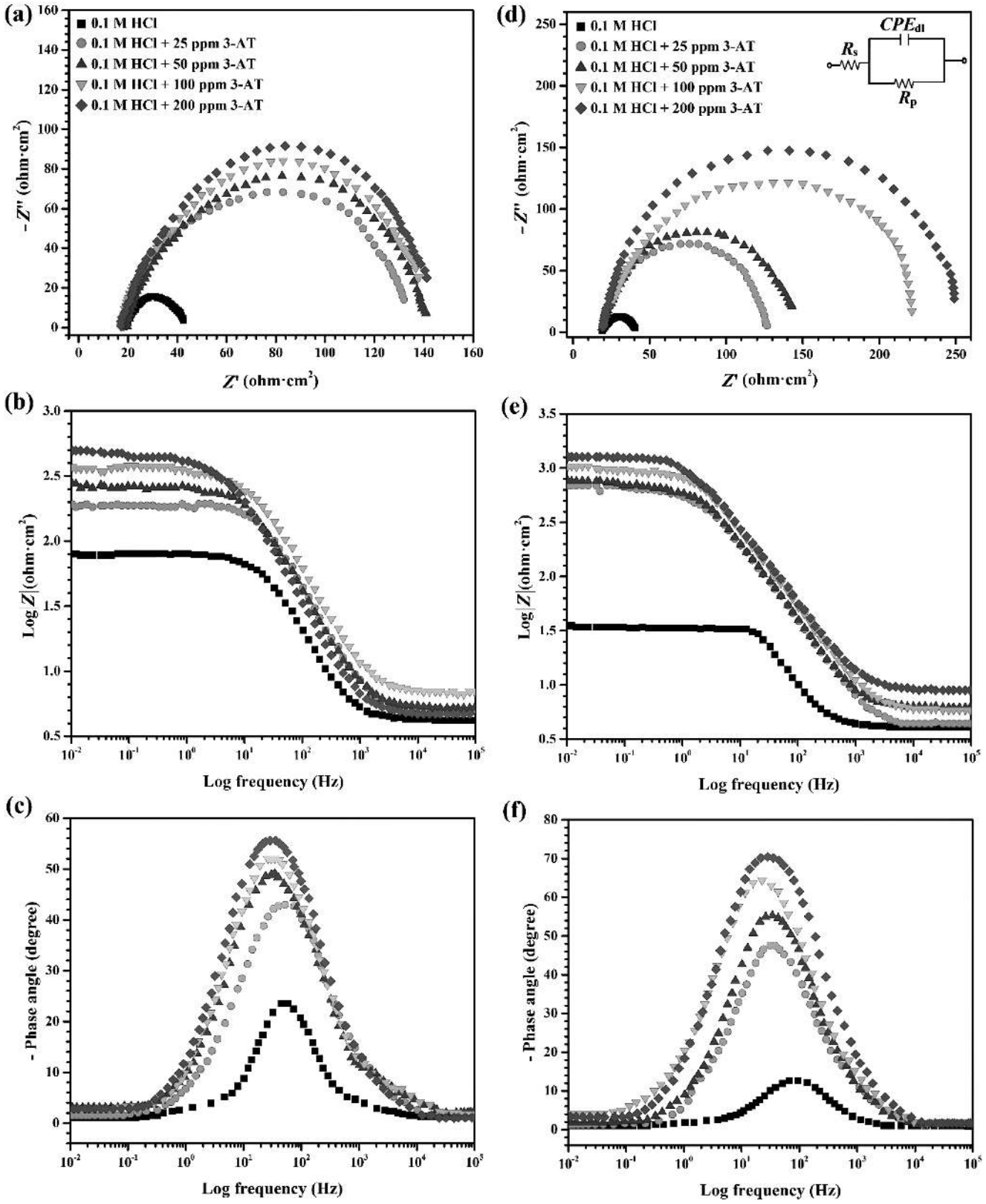


Fig. 9. Nyquist and Bode plots of (a–c) Ref and (d–f) WB samples in 0.1 M HCl without and with various concentrations of 3-AT. Equivalent circuit for the EIS data has been shown as inset in (d).

Comparison between nanocrystalline (WB) and coarse-grained (Ref) morphologies in the presence of inhibitor indicates that for nanocrystalline structure, the polarization resistances in the presence of inhibitor are reasonably increased and its capacitances are decreased. This may result from a decrease in local dielectric constant and/or an increase in the thickness of the electrical double layer, suggesting that active sites of nanostructured surfaces encourage the adsorption of 3-AT molecules. Considering the EIS results and comparing them with the polarization results at various concentrations of inhibitors, it can be clearly understood that the surface nanocrystallization improves the inhibition efficiency of 3-AT.

### 3.2.2. Effect of temperature

In order to assess the effect of temperature on the corrosion rate of specimens, potentiodynamic polarization testing was performed at temperatures from 30 to 60 °C in the absence and presence of optimum concentration of 3-AT (200 ppm, most effective concentration). Table 5 shows the electrochemical parameters corresponding to polarization results at various temperatures in 0.1 M HCl solution. These results clearly show that inhibitive effect for all conditions decreases with increasing the solution temperature, which can be attributed to the quick desorption of adsorbed inhibitor molecules from the surface in addition to the decomposition of these molecules at elevated temperatures [37, 40, 42]. Nonetheless the corrosion rate of inhibited solution is always lower than the blank one. In addition, comparing the Ref and WB samples in the presence of 200 ppm of 3-AT reveals that enhanced inhibitor adsorption for WB coupon leads to lower iron dissolution at high temperature so that its corrosion rate at 60 °C is about 0.60 mA · cm$^{-2}$.

In order to better understand the significance of temperature on iron dissolution from WB and Ref coupons in these solutions, the Arrhenius equation can be employed:

$$\ln(i_{corr}) = \ln A - \frac{E_a}{RT} \quad (7)$$

Which $i_{corr}$, $A$, $R$, $T$ and $E_a$ are the corrosion current density, Arrhenius pre-exponential factor, gas constant, absolute temperature and activation energy, respectively. By plotting $\ln(i_{corr})$ vs. $1/T$, $E_a$ values can be obtained (see Fig. 10 and Table 6). Assessing the $E_a$ values reveals two points:

1. Since higher $E_a$ in the presence of inhibitors in comparison with blank solution typically implies physisorption [44], 3-AT has an electrostatic character (physisorption) on the Ref and WB surfaces. In addition, higher $E_a$ values for the inhibited solutions meaning that the strong inhibition action of 3-AT leads to a high energy barrier for the corrosion process.

2. The enhanced presence of active sites on the surface of the WB coupon is a reason for its low $E_a$ value in the absence of corrosion inhibitor. However, these sites can serve as ideal positions for more adsorption of 3-AT. High activation energy for WB in inhibited solution ( ~ 72.22 kJ · mol$^{-1}$) is evidence for this claim.

Table 4. Impedance parameters for Ref and WB coupons in 0.1 M HCl without and with different concentrations of 3-AT.

| Sample | Inhibitor concentration | $R_s$ ($\Omega \cdot cm^2$) | $R_p$ ($\Omega \cdot cm^2$) | $CPE_{dl}$ | | $C_{dl}$ ($\mu F \cdot cm^{-2}$) | $\chi^2 \times 10^{-5}$ | $\%\eta_p$ |
|---|---|---|---|---|---|---|---|---|
| | | | | $P$ ($\mu F \cdot cm^{-2}$) | $n$ | | | |
| Ref | 0 | 19 | 25 | 462 | 0.86 | 403.14 | 10.1 | – |
| | 25 | 18 | 111 | 159 | 0.85 | 137.78 | 24.6 | 77.5 |
| | 50 | 18 | 121 | 126 | 0.86 | 110.04 | 18.3 | 79.3 |
| | 100 | 18 | 130 | 118 | 0.87 | 103.87 | 17.7 | 80.8 |
| | 200 | 18 | 143 | 121 | 0.86 | 105.68 | 20.4 | 82.5 |
| WB | 0 | 20 | 20 | 511 | 0.82 | 433.05 | 12.5 | – |
| | 25 | 110 | 110 | 106 | 0.84 | 91.12 | 19.5 | 81.8 |
| | 50 | 131 | 134 | 104 | 0.81 | 87.54 | 32.5 | 85.1 |
| | 100 | 196 | 196 | 95 | 0.83 | 81.06 | 28.9 | 89.8 |
| | 200 | 236 | 236 | 76 | 0.80 | 63.56 | 25.8 | 91.5 |

Table 5. Corrosion rate of Ref and WB coupons in 0.1 M HCl in the absence (blank) and presence 200 ppm of 3-AT (inhibited solution) at various temperatures.

| Temperature (°C) | Corrosion rate, Ref (mA · cm$^{-2}$) | | Corrosion rate, WB (mA · cm$^{-2}$) | |
|---|---|---|---|---|
| | Blank | Inhibited solution | Blank | Inhibited solution |
| 30 | 0.90 | 0.12 | 1.26 | 0.05 |
| 40 | 1.52 | 0.19 | 1.71 | 0.11 |
| 50 | 2.03 | 0.37 | 2.24 | 0.29 |
| 60 | 3.14 | 0.85 | 3.22 | 0.60 |

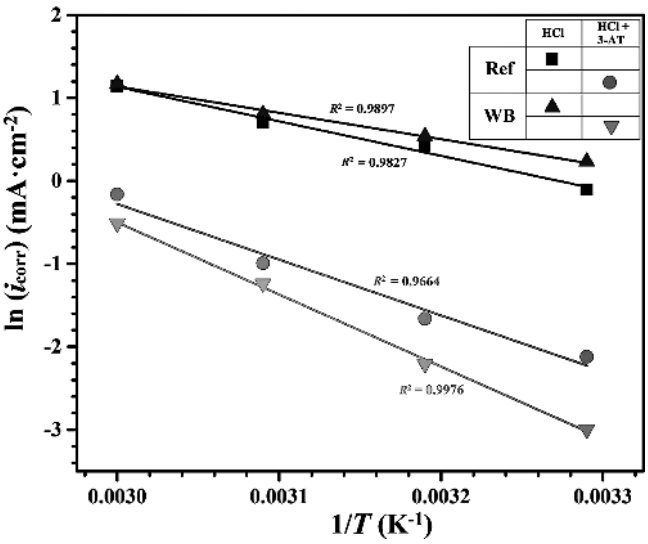


Fig. 10. $\ln(i_{corr})$ vs. $1/T$ for mild steel coupons in 0.1 M HCl in the absence and presence of 200 ppm of 3-AT.

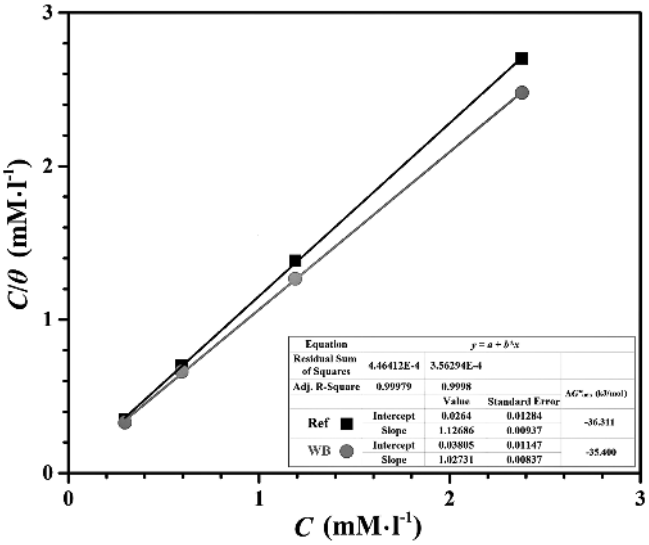


Fig. 11. Langmuir isotherm plots for the adsorption of 3-AT on the surface of Ref and WB coupons in 0.1 M HCl.

Table 6. Activation parameter and change in standard free energy for the adsorption of 3-AT on the surface of Ref and WB coupons.

| Sample | $E_a$ (kJ · mol $^{-1}$) | | $\Delta G^\circ_{ads}$ (kJ · mol $^{-1}$) |
|---|---|---|---|
| | Blank solution | Inhibited solution | |
| Ref | 34.59 | 55.85 | –36.311 |
| WB | 26.39 | 73.16 | –35.400 |

### 3.2.3. Adsorption characteristics of the inhibitors

To gain insight into the inhibition mechanism, having a clear understanding of the basic thermodynamic information on the interaction between inhibitor molecules and metal surface is necessary. Adsorption of the inhibitor molecule on the metal surface may be chemisorption, physisorption or physiochemisorption. The type of inhibitor adsorption can be determined using thermodynamic data obtained from isotherms. There are several adsorption isotherms such as Langmuir, Temkin, Bockris–Swinkels, Flory–Huggins and Frumkin [37]. A typical adsorption process involves the replacement of the adsorbed water molecule ($H_2O_{ads}$) by inhibitor molecules present in aqueous solution ($Org_{aq}$) at the metal/electrolyte interface as represented below [45]:

$$Org_{sol} + xH_2O_{ads} \leftrightarrow Org_{ads} + xH_2O_{sol} \quad (8)$$

In the above reaction, $x$ is the number of water molecules replaced by one molecule of organic inhibitor. The mentioned isotherms were tested and the Langmuir adsorption isotherm gave the best fit, with values of the regression coefficient very close to 1. Based on this isotherm, the surface coverage ($\theta$) is proportional to inhibitor concentration ($C$) as follows [42]:

$$\frac{C}{\theta} = \frac{1}{K_{ads}} + C \quad (9)$$

Where $C$ is the inhibitor concentration, $\theta$ is surface coverage and $K_{ads}$ is the equilibrium constant for adsorption reaction. By plotting the $C/\theta$ vs. $C$ (Fig. 11), $K_{ads}$ which is equal to the inverse of the intercept, can be obtained. The $K_{ads}$ is related to the standard free energy ($\Delta G^\circ_{ads}$) of adsorption process by [45]:

$$\Delta G^\circ_{ads} = -RT\ln(55.5K_{ads}) \quad (10)$$

Where $R$ is the gas constant, $T$ is the absolute temperature in Kelvin and the numerical value 55.5 represents the water molar concentration in acid solution. Values of $\Delta G^\circ_{ads}$ around –20 kJ · mol$^{-1}$ or less negative have been attributed to electrostatic interactions between the charged adsorbate molecules and the charged metal surface while values around –40 kJ · mol$^{-1}$ or more negative involve charge transfer from organic molecules to the metal surface to form coordinate bonds (chemisorption) [46]. For both Ref and WB coupons immersed in inhibited solution (0.1 HCl + 200 ppm 3-AT), the values of $\Delta G^\circ_{ads}$ have negative sign which in turn refer to the adsorption of inhibitors onto the surface of samples (see Fig. 11 and Table 6). $\Delta G^\circ_{ads}$ values are similar for Ref and WB, meaning that the spontaneity of adsorption reaction is not affected by surface nanocrystallization.

## 4. Conclusions

The important conclusions derived from the study are summarized as follows:

1. Surface nanocrystallization increases the corrosion rate of mild steel in 0.1 M HCl solution. This is directly related to the increment of the amount of atoms that take part in the corrosion reaction.
2. 3-AT shows good inhibitive performance for both annealed and wire brushed coupons so that an increase in its concentration gives a noticeable improvement in the inhibition efficiency.
3. In the presence of 3-AT corrosion inhibitor, the WB coupon with a nanocrystalline surface layer shows a superior corrosion performance compared with the Ref one. This is attributed to the increased number of active

sites (grain boundaries) on the WB coupon which can serve as good positions for inhibitor adsorption.

4. Comparison of EIS results for Ref and WB coupons shows that for WB the polarization resistance increases more in the presence of corrosion inhibitor and its capacitance decreases more. These higher polarization resistance and lower double layer capacitance of WB can be respectively attributed to the effective adsorption of 3-AT and decrease in local dielectric constant.
5. Increasing the temperature promotes desorption of 3-AT from the Ref and WB surfaces, however its effect on the WB coupon is not as impressive as on the Ref one.
6. For both Ref and WB coupons, adsorption of 3-AT obeys the Langmuir isotherm, showing physisorption onto the mild steel surface.
7. Based on the thermodynamic calculations, although 3-AT adsorbs spontaneously on micro- and nanocrystalline surfaces, the spontaneity of the adsorption reaction is independent of surface grain size.

The authors thank Mr. Hashem Teimourinjad, Mr. Afshin Nazarnejatizadeh (experts in metallurgy and Drawing units at KSTC), Mr. Mohsen Norouzi and Dr. Saeed Abbasizadeh for their great helps in the practical works.

**References**

[1] T. Burakowski, T. Wierzchon: Surface engineering of metals: principles, equipment, technologies, CRC press, Connecticut (1998).
[2] J.R. Davis: Surface engineering for corrosion and wear resistance, ASM international, Ohio (2001).
[3] S. Li, Y. Zuo, P. Ju: Appl. Surf. Sci. 331 (2015) 200. DOI:10.1016/j.apsusc.2015.01.087
[4] A.S. Hamada, P. Sahu, D.A. Porter: Appl. Surf. Sci. 356 (2015) 1. DOI:10.1016/j.apsusc.2015.07.153
[5] S. Pour-Ali, C. Dehghanian, A. Kosari: Corros. Sci. 85 (2014) 204. DOI:10.1016/j.corsci.2014.04.018
[6] V. Malinovschi, A. Marin, S. Moga, D. Negrea: Surf. Coat. Technol. 253 (2014) 194. DOI:10.1016/j.surfcoat.2014.05.036
[7] Y. Wang, J. Zeng: Surf. Coat. Technol. 245 (2014) 55. DOI:10.1016/j.surfcoat.2014.02.040
[8] W.H. Liu, F.S. Shieu, W.T. Hsiao: Surf. Coat. Technol. 249 (2014) 24. DOI:10.1016/j.surfcoat.2014.03.041
[9] T.F. Zhang, Q.Y. Deng, B. Liu, B.J. Wu, F.J. Jing, Y.X. Leng, N. Huang: Surf. Coat. Technol. 273 (2015) 12. DOI:10.1016/j.surfcoat.2015.03.031
[10] G. Telasang, J. Dutta Majumdar, G. Padmanabham, I. Manna: Surf. Coat. Technol. 261 (2015) 69. DOI:10.1016/j.surfcoat.2014.11.058
[11] L. Ge, N. Tian, Z. Lu, C. You: Appl. Surf. Sci. 286 (2013) 412. DOI:10.1016/j.apsusc.2013.09.105
[12] Z. Tong, Z.M. Shi, S.J. Tong, D.W. Wang, P.F. Li: Surf. Coat. Technol. 251 (2014) 293. DOI:10.1016/j.surfcoat.2014.04.042
[13] S. Bagherifard, I. Fernandez-Pariente, R. Ghelichi, M. Guagliano: Mater. Des. 45 (2013) 497. DOI:10.1016/j.matdes.2012.09.025
[14] H. Gleiter: Acta Mater. 45 (2000) 1. DOI:10.1016/S1359-6454(99)00285-2
[15] X.C. Liu, H.W. Zhang, K. Lu: Acta Mater. 96 (2015) 24. DOI:10.1016/j.actamat.2015.06.014
[16] D. Hughes, N. Hansen: Phys. Rev. Lett. 87 (2001) 135503. DOI:10.1103/PhysRevLett.87.135503
[17] D. Song, A. Ma, W. Sun, J. Jiang, J. Jiang, D. Yang, G. Guo: Corros. Sci. 82 (2014) 437. DOI:10.1016/j.corsci.2014.01.034
[18] H. Kitahara, T. Yada, M. Tsushida, S. Ando: Procedia Eng. 10 (2011) 2737. DOI:10.1016/j.proeng.2011.04.456
[19] E. Oguzie, Y. Li, F. Wang: Electrochim. Acta 52 (2007) 6988. DOI:10.1016/j.electacta.2007.05.023
[20] V. Afshari, C. Dehghanian: Int. J. Mater. Res. 101 (2010) 366. DOI:10.3139/146.110289
[21] Y. Li, F. Wang, G. Liu: Corrosion 60 (2004) 891. DOI:10.5006/1.3287822
[22] W. Luo, Y. Xu, Q. Wang, P. Shi, M. Yan: Corros. Sci. 52 (2010) 3509. DOI:10.1016/j.corsci.2010.06.029
[23] R. Mishra, R. Balasubramaniam: Corros. Sci. 46 (2004) 3019. DOI:10.1016/j.corsci.2004.04.007
[24] Y.W. Hao, B. Deng, C. Zhong, Y.M. Jiang, J. Li: J. Iron Steel Res. Int. 16 (2009) 68. DOI:10.1016/S1006-706X(09)60030-3
[25] X.Y. Wang, D.Y. Li: Wear 255 (2003) 836. DOI:10.1016/S0043-1648(03)00055-3
[26] K. Ralston, N. Birbilis: Corrosion 66 (2010) 075005-1. DOI:10.5006/1.3462912
[27] E. Oguzie, S. Wang, Y. Li, F. Wang: J. Solid State Electrochem. 12 (2008) 721. DOI:10.1007/s10008-007-0415-0
[28] E. Oguzie, S. Wang, Y. Li, F. Wang: J. Phys. Chem. C 113 (2009) 8420. DOI:10.1021/jp9015257
[29] S. Umoren, Y. Li, F. Wang: J. Mater. Environ. Sci. 1 (2010) 189.
[30] S. Umoren, Y. Li, F. Wang: Corros. Sci. 53 (2011) 1778. DOI:10.1016/j.corsci.2011.01.052
[31] A. Khorsand Zak, W.H. Abd. Majid, M.E. Abrishami, R. Yousefi: Solid State Sci. 13 (2011) 251. DOI:10.1016/j.solidstatesciences.2010.11.024
[32] P. Joshi, P. Ramakrishnan: Materials for Electrical and Electronic Contacts: Processing, Properties, and Applications, Science Pub Inc, Enfield (2004).
[33] E.J. Mittemeijer, P. Scardi: Diffraction analysis of the microstructure of materials, Springer Science & Business Media, Berlin (2013).
[34] N.R. Tao, Z.B. Wang, W.P. Tong, M.L. Sui, J. Lu, K. Lu: Acta Mater. 50 (2002) 4603. DOI:10.1016/S1359-6454(02)00310-5
[35] B.D. Cullity: Elements of X-ray diffraction, Addison-Wesley Pub. Co., Boston, USA (1956).
[36] S. Bagherifard, M. Guagliano: Eng. Fract. Mech. 81 (2012) 56. DOI:10.1016/j.engfracmech.2011.06.011
[37] A. Kosari, M. Momeni, R. Parvizi, M. Zakeri, M.H. Moayed, A. Davoodi, H. Eshghi: Corros. Sci. 53 (2011) 3058. DOI:10.1016/j.corsci.2011.05.009
[38] E. McCafferty: Introduction to corrosion science, Springer Science & Business Media, New York (2010). DOI:10.1007/978-1-4419-0455-3
[39] V. Afshari, C. Dehghanian: Mater. Chem. Phys. 124 (2010) 466. DOI:10.1016/j.matchemphys.2010.06.067
[40] J. Saranya, M. Sowmiya, P. Sounthari, K. Parameswari, S. Chitra, K. Senthilkumar: J. Mol. Liq. 216 (2016) 42. DOI:10.1016/j.molliq.2015.12.096
[41] S. Pour-Ali, A. Kiani-Rashid, A. Babakhani, A. Davoodi: Appl. Surf. Sci. 376 (2016) 121. DOI:10.1016/j.apsusc.2016.03.131
[42] C. Verma, E. Ebenso, I. Bahadur, I. Obot, M. Quraishi: J. Mol. Liq. 212 (2015) 209. DOI:10.1016/j.molliq.2015.09.009
[43] S. Ullah, M.A. Bustam, A.M. Shariff, G. Gonfa, K. Izzat: Appl. Surf. Sci. 365 (2016) 76. DOI:10.1016/j.apsusc.2015.12.232
[44] A. Kosari, M.H. Moayed, A. Davoodi, R. Parvizi, M. Momeni, H. Eshghi, H. Moradi: Corros. Sci. 78 (2014) 138. DOI:10.1016/j.corsci.2013.09.009
[45] C. Verma, M. Quraishi, A. Singh: J. Mol. Liq. 212 (2015) 804. DOI:10.1016/j.molliq.2015.10.026
[46] L.O. Olasunkanmi, M.M. Kabanda, E.E. Ebenso: Physica E 76 (2016) 109. DOI:10.1016/j.physe.2015.10.005

(Received May 9, 2016; accepted August 11, 2016; online since September 29, 2016)

**Correspondence address**

Dr. Sadegh Pour-Ali
Materials and Metallurgical Engineering Department
Faculty of Engineering, Ferdowsi University of Mashhad
91775-1111, Mashhad
Iran
Tel.: +98 513 8817182
Fax: +98 513 8807182
E-mail: Pourali2020@ut.ac.ir, Babakhani@um.ac.ir

**Bibliography**
DOI 10.3139/146.111432
Int. J. Mater. Res. (formerly Z. Metallkd.)
107 (2016) 11; page 1031 – 1040

ISSN 1862-5282